3-D impedance networks simulate complex resistivity spectra of sand-pyrite-water mixtures

Maineult, Alexis; Weller, Andreas; Martin, Tina; Titov, Konstantin; Florsch, Nicolas

Published in:
Geophysical Journal International

DOI:
10.1093/gji/ggaf269

2025

Document Version:
Publisher's PDF, also known as Version of record

Geophysical Journal International

Geophys. J. Int. (2025) **242,** 1–17
Advance Access publication 2025 July 12
Rock and Mineral Physics, Rheology

https://doi.org/10.1093/gji/ggaf269

3-D impedance networks simulate complex resistivity spectra of sand-pyrite-water mixtures

Alexis Maineult [1], Andreas Weller [2], Tina Martin [3], Konstantin Titov [4] and Nicolas Florsch [5]

[1] *Laboratoire de Géologie, Ecole Normale Supérieure / CNRS UMR*8538, *PSL Research University,* F-75005 *Paris, France. E-mail: alexis.maineult@ens.fr*
[2] *Institute of Geotechnology and Mineral Resources, Clausthal University of Technology,* D-38678 *Clausthal-Zellerfed, Germany*
[3] *Division of Engineering Geology, Lund University,* SE-22363 *Lund, Sweden*
[4] *St. Petersburg State University, Institute of Earth Sciences,* 199034 *St. Petersburg, Russia*
[5] *Sorbonne Université, Institut de Recherche pour le Développement, Unité de Modélisation Mathématique et Informatique des Systèmes Complexes,* F-75005 *Paris, France*

Accepted 2025 July 11. Received 2025 June 24; in original form 2025 March 15

SUMMARY

Characterizing ore deposits or mining dumps in terms of mineral content and grain size remains a challenge. Since the 1950s the induced polarization (IP) method has been successfully applied in ore prospecting. However, reliably interpreting field survey data requires comprehensive laboratory studies to establish a link between the IP parameters from empirical or phenomenological models and the type and quantity of ore minerals. In this study, we use numerical electrical networks to replicate the complex electrical resistivity spectra observed in experiments on sand-pyrite-water mixtures. A network consists of a 3-D assembly of resistors, representing the saturated pore space and leaky capacitors simulating the electrical behaviour of ore minerals. A sophisticated fitting procedure enables the precise determination of resistor and capacitor parameters, ultimately leading to strong agreement between measured and synthetic IP spectra. The results obtained from the 3-D network align well with the classical Pelton model, which is based on a simple equivalent circuit. Our findings indicate that the network's chargeability depends on the fraction of capacitors in the system (i.e. the number of capacitors divided by the number of capacitors and resistors), and that the Pelton time constant of the measured spectra is closely related to the resistor and capacitor parameters. We argue that a 3-D approach offers a more realistic framework, paving the way for future studies on the effects of ore grain size distribution, and the spatial arrangement of ore grains.

Key words: Electrical properties; Induced polarization; Numerical modelling.

1 INTRODUCTION

The global demand for metallic resources is increasing, driven by the development of technologies essential for the energy transition. As a result, exploration efforts must expand to include a broader range of mineral resource types. Some of these minerals, previously overlooked, are found in mining and processing dumps as residual by-products. In addition to new ore deposits, the raw material potential of these dumps is becoming a key focus in exploration strategies. This growing interest underscores the urgent need for advanced prospecting technologies capable of reassessing mining and processing dumps in terms of mineral composition and content.

Surface geophysical methods, particularly geoelectrical techniques, are well-suited for this challenge due to their non-invasive nature and ability to provide dense spatial sampling of study areas. Among these, the induced polarization (IP) method has been widely used in ore exploration since the 1950s (Seigel *et al.* 2007). IP extends the classical geoelectrical method, which primarily focuses on the DC electrical resistivity of soils and rocks. In addition to measuring the resistivity, IP records the chargeability of materials, that is, their ability to reversibly store electrical charges. The high chargeability of many ore minerals forms the basis for the successful application of IP in mineral prospecting.

A reliable interpretation of field survey data relies on empirical, phenomenological or mechanistic models that establish a relationship between model parameters and the type and quantity of ore minerals. The development and validation of models linking IP parameters to the underlying polarization mechanisms remain an ongoing research effort. Moreover, these models must be calibrated through comprehensive laboratory studies that systematically examine the influence of key factors, such as metallic particle content, grain size, grain shape and fluid conductivity, under controlled conditions.

Accurately computing the complex resistivity response of metallic grains embedded in a non-polarizing medium, such as sand–water mixture, remains a challenge. Significant progress has been made in developing advanced numerical models that account for the electrochemical origins of polarization at the surface of metallic particles (e.g. Wong 1979; Abdulsamad *et al.* 2017; Bücker *et al.* 2018; Kreith *et al.* 2025). However, despite these advancements, existing models still fail to fully capture all the effects observed in experimental studies.

Given the limitations of existing theoretical models, phenomenological approaches remain a valuable tool for realistically describing IP spectra. Since the seminal work of Pelton *et al.* (1978), equivalent electrical circuits have been widely used as an effective modelling framework. Pelton *et al.* (1978) formulated an equation to describe the complex impedance spectra using a simple model consisting of a fluid-filled pore in parallel with a pore blocked by a metallic grain. The resulting four-parameter Pelton model—comprising DC-resistivity, chargeability, time constant and frequency exponent—has been extensively adopted due to its simplicity and its ability to fit a broad range of observed complex resistivity spectra at both sample and field scales. To extend the phenomenological description to a wider range of spectra, the Pelton model has been generalized and modified over time (e.g. Pelton *et al.* 1983; Dias 2000). Additionally, questions regarding model equivalence have been explored (e.g. Weller & Slater 2022).

A key question arises: Can a model with only two distinct pores in parallel accurately represent a sample containing a large number of pores? To address this, we propose to apply network modelling following the approach of Maineult *et al.* (2017, corrected by Maineult 2018). They developed a 2-D impedance network for the numerical simulation of complex resistivity spectra in material with varying pore radius distributions. Using this network modelling algorithm, Maineult *et al.* (2018) simulated the IP response during drainage and imbibition processes, while Mendieta *et al.* (2023) predicted the shape of IP spectra for mixtures containing different types of clay. Additionally, Stebner *et al.* (2017) employed 3-D network modelling to investigate the effects of membrane polarization.

In our study, we extend the 2-D approach of Maineult *et al.* (2017) to a 3-D network that simulates the IP spectra of samples containing metallic particles dispersed in water-saturated sand. Fortunately, numerous studies have reported laboratory IP measurements on mixtures with metallic particles (e.g. Grissemann 1971; Pelton *et al.* 1978; Nordsiek & Weller 2008; Gurin *et al.* 2013; Placencia-Gomez *et al.* 2013; Hupfer *et al.* 2016; Abdulsamad *et al.* 2017; Martin & Weller 2023). Using our 3-D numerical network modelling approach, we successfully reproduce the IP spectra of pyrite-sand-water mixtures reported by Hupfer *et al.* (2016) and Martin & Weller (2023). In a second step, we analyse the relationship between IP parameters at the sample scale and the parameters of the network elements, which are intended to represent the electrical properties at the pore and grain scale.

2 THEORY

2.1. Principle of spectral induced polarization

The spectral induced polarization (SIP) method involves injecting a sinusoidal electrical current I of various frequencies f, typically ranging from 1 mHz to 10 kHz, into a medium via two current electrodes. The resulting electrical potential difference ΔV is then measured between two potential electrodes (e.g. Binley & Slater 2020). The frequency-dependent apparent complex resistivity is given by:

$$\rho^*(f) = K\frac{\Delta V(f)}{I(f)}, \tag{1}$$

where K is a geometric factor that depends on the positions of the current and potential electrodes. Since ρ^* is a complex quantity, it can be expressed as:

$$\rho^*(f) = \rho(f)\exp(i\varphi(f)), \tag{2}$$

where $\rho(f)$ represents the amplitude spectrum and $\varphi(f)$ the phase spectrum.

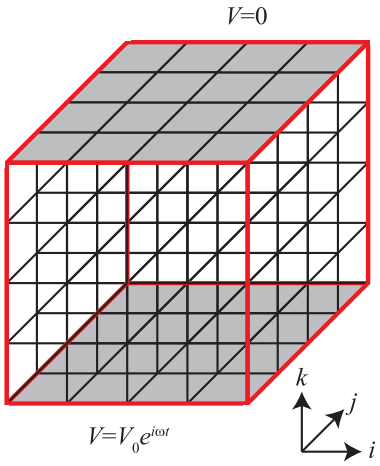

Figure 1. Cubic network. Each link is associated with an impedance. A potential difference is applied between the top and bottom faces, while no current flows through the lateral faces. The voltage difference is equal to $V_0\exp(i\omega t)$, where V_0 is a fixed amplitude, ω the angular frequency and t the time.

2.2. Numerical computation of the SIP response of a cubic network of complex impedances

Fig. 1 illustrates a cubic electrical network consisting of N_i N_j N_k nodes, where each link between neighbouring nodes represents a complex impedance. An electrical potential of $V_0\exp(i\omega t)$ is applied to the bottom face, while the top face is set to zero potential (both shown in grey in Fig. 1). No normal current flux is allowed to the four remaining faces.

Applying Kirchhoff's law at each internal node (i,j,k), we obtain:

$$I_{(i-1,j,k)\to(i,j,k)} + I_{(i,j,k)\to(i+1,j,k)} + I_{(i,j-1,k)\to(i,j,k)} + I_{(i,j,k)\to(i,j+1,k)} + I_{(i,j,k-1)\to(i,j,k)} + I_{(i,j,k)\to(i,j,k+1)} = 0, \tag{3}$$

where $I_{p\to q}$ represents the electrical current between node p and node q. By applying Ohm's law, eq. (3) transforms into:

$$\frac{V_{i,j,k}-V_{i-1,j,k}}{Z_{(i-1,j,k)\to(i,j,k)}} + \frac{V_{i+1,j,k}-V_{i,j,k}}{Z_{(i,j,k)\to(i+1,j,k)}} + \frac{V_{i,j,k}-V_{i,j-1,k}}{Z_{(i,j-1,k)\to(i,j,k)}} + \frac{V_{i,j+1,k}-V_{i,j,k}}{Z_{(i,j,k)\to(i,j+1,k)}} + \frac{V_{i,j,k}-V_{i,j,k-1}}{Z_{(i,j,k-1)\to(i,j,k)}} + \frac{V_{i,j,k+1}-V_{i,j,k}}{Z_{(i,j,k)\to(i,j,k+1)}} = 0, \tag{4}$$

where $V_{i,j,k}$ stands for the electrical potential at node (i,j,k), and $Z_{p\to q}$ is the impedance associated with the link between nodes p

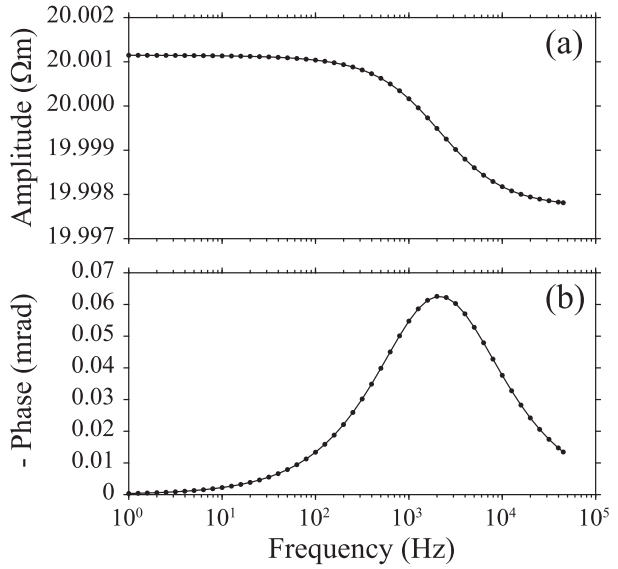

Figure 2. Complex resistivity spectra [amplitude (a) and phase (b)] of a 30 × 30 × 30 network containing a single capacitor at its centre, aligned with the potential gradient direction ($R = 100\,000\ \Omega$, $C = 10^{-10}$ F, $c = 0.8$, $L = 200$ μm). Dots represent the computed results, while lines correspond to the Pelton model fitting ($\rho_0 = 20.001\ \Omega$m, $m = 1.724\ 10^{-4}$, $\tau_P = 7.478\ 10^{-5}$ s, $c_P = 0.8$).

and q. For the nodes located on the network's boundary faces, eq. (4) is modified to account for the boundary conditions described above. The resulting set of $N_i\ N_j\ N_k$ equations forms a complex linear system in V for a given frequency $f = \omega/(2\pi)$. Once this system is solved (as in Maineult *et al.* 2017, see their eqs 9 to 11), we can determine the resistivity amplitude ρ and of the phase φ for the considered frequency f, as (see Maineult *et al.* 2017 for further details):

$$\rho = \frac{N_i N_j L^2}{(N_k - 1)\,L} \frac{|\Delta V|}{\sum_{i=1}^{N_i}\sum_{j=1}^{N_j} I_{(i,j,1)\rightarrow(i,j,2)}} = \frac{N_i N_j L}{(N_k - 1)} \frac{V_0}{\sum_{i=1}^{N_i}\sum_{j=1}^{N_j} I_{(i,j,1)\rightarrow(i,j,2)}} \tag{5}$$

and

$$\varphi = -\arg\left(\sum_{i=1}^{N_i}\sum_{j=1}^{N_j} I_{(i,j,1)\rightarrow(i,j,2)}\right), \tag{6}$$

where L represents the characteristic length of the cubic mesh, that is, the distance between two adjacent nodes. The procedure is repeated for the entire set of required frequencies.

2.3. Complex impedances for the sand-pyrite-water mixture

As in the Pelton model (Pelton *et al.* 1978), we assume that a sand-pyrite-water mixture can be represented using only two types of impedances: perfect resistors and leaky capacitors. However, unlike Pelton *et al.* (1978), we do not distinguish between free pores and pores blocked by a pyrite grain. Instead, we classify the network into two types of links: 'passive links' and 'active links'. On one hand, passive links correspond to water-filled pores, which are purely conductive and therefore modelled as resistors with impedance R. Active links, on the other hand, represent pyrite grains, which are treated as leaky capacitors. In a first approximation, we neglect their resistance and assign them an impedance of the form $(i\omega C)^{-c}$, where C is the capacitance (in F). The exponent c ($0 < c \leq 1$) characterizes the degree of capacitor imperfection: $c = 1$ for an ideal capacitor, and $0 < c < 1$ to account for leakage through the capacitor.

For all the results presented hereafter, we make two additional assumptions: (1) All pores are considered identical, meaning they have the same length L and the same resistance R. (2) All pyrite grains are assumed to be identical, having the same capacitance C and the same exponent c.

2.4. The Pelton model and fitting procedure

Based on the assumption that a sand-pyrite-water mixture can be modelled as an electrical circuit, where a resistor represents a free water-saturated pore and is placed in parallel with a series combination of a resistor and a leaky capacitor representing a water-filled pore blocked by a pyrite grain, Pelton *et al.* (1978) proposed the following formula for the complex resistivity of such a circuit:

$$\rho_P^* = \rho_0\left(1 - m\left(1 - \frac{1}{1 + (i\omega\tau_P)^{c_P}}\right)\right), \tag{7}$$

where ρ_0 is the DC resistivity, m the chargeability, τ_P a model-specific time constant and c_P the Cole-Cole exponent, which ranges between 0 and 1 (Cole & Cole 1941). To compare the parameters obtained from our simulation with those of the Pelton model, we developed an optimization procedure based on the simulated annealing (see for instance, Maineult 2016, but without the monotonicity constraint), followed by a refinement using the simplex method (Nelder & Mead 1965). This approach allows us to determine the optimal values of ρ_0, m, τ_P and c_P for a given complex resistivity spectrum. The cost-function F used in this procedure is derived from the adjustment coefficients for the resistivity amplitude ρ and the phase φ, and is defined as follow:

$$F = \frac{\sum_{j=1}^{Na}\left(\rho_j^{\text{observed}} - \rho_j^{\text{predicted}}\right)^2}{\sum_{j=1}^{Na}\left(\rho_j^{\text{observed}} - \langle\rho^{\text{observed}}\rangle\right)^2} + \frac{\sum_{j=1}^{Np}\left(\varphi_j^{\text{observed}} - \varphi_j^{\text{predicted}}\right)^2}{\sum_{j=1}^{Np}\left(\varphi_j^{\text{observed}} - \langle\varphi^{\text{observed}}\rangle\right)^2}. \tag{8}$$

3 NUMERICAL SIMULATIONS

First, we examine the effect of a single leaky capacitor embedded in a resistive medium. To do so, we placed a single active link at the centre of a 30 × 30 × 30 network composed entirely of passive links. When the active link is aligned with the main direction of the electrical current (i.e. perpendicularly to the two end-faces where the potential is imposed, along the k-direction, Fig. 1), it produces a 'classical' spectrum (shown in Fig. 2) that can be perfectly fitted by the Pelton model (eq. 7), albeit with a low chargeability. Notably, the fitted c_P value matches the c value assigned to the leaky capacitor (i.e. 0.8). Conversely, when the active link is orientated along the i- or j- direction (parallel to the two end-faces where the potential is imposed), no polarization is observed. Instead, the amplitude spectrum remains flat at 20 Ωm (not shown

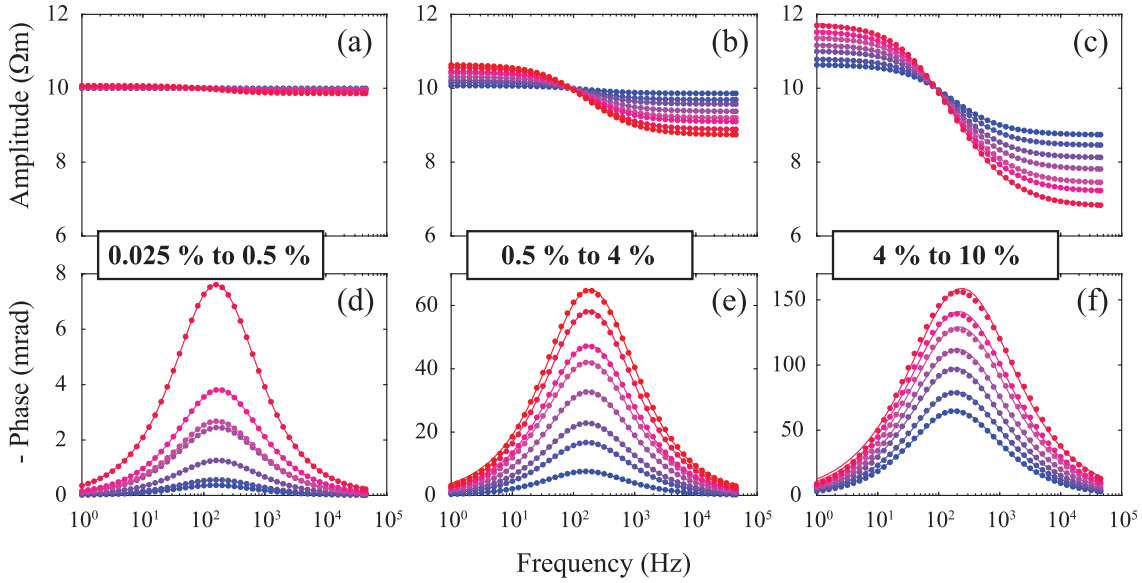

Figure 3. Effect of the fraction of capacitors (f_C) in the network on the resistivity amplitude (a, b, c) and phase (d, e, f). Dots represent the computed results for $30 \times 30 \times 30$ networks ($R = 50\,000\ \Omega$, $C = 10^{-8.5}$ F, $c = 0.8$, $L = 200\ \mu$m), while lines correspond to the Pelton model fitting. On each graph, blue shades indicate the lowest f_C values, red shades the highest, with f_c varying from 0.025 per cent to 0.5 per cent (a, d), 0.5 per cent to 4 per cent (b, e) and 4 per cent to 10 per cent (c, f).

here), indicating that the current lines are perfectly aligned with the k direction.

To simulate an increase in pyrite content within the mixture, we generate networks in which active links are randomly distributed. The results shown in Fig. 3 demonstrate that polarization effects intensify with increasing fraction of capacitors f_C, which corresponds to the number of capacitors normalized to the total number of circuit elements in the network (equal to the number of capacitors plus number of resistors). The resulting spectra can still be accurately fitted using the Pelton model up to a fraction of 6 per cent. However, for higher f_C values, the fit quality decreases, particularly near the phase peak.

The DC resistivity ρ_0 is directly proportional to f_C, increasing with higher pyrite content, as shown in Fig. 4(a). When the frequency tends towards 0, the behaviour of a capacitor is equivalent to an infinite resistance: as a consequence, increasing the number of resistors causes an increase of the resistivity ρ_0. Fig. 4(b) illustrates the continuous increase of chargeability. Notably, the slope of the linear relationship between chargeability and the fraction of capacitors f_C is 4.355, which is intriguingly close to 9/2. This value has been reported by Revil *et al.* (2015) as approximation for the relationship between chargeability and the volume fraction of metallic particles that has been derived from the effective medium theory with different mixing equations (e.g. Gurin *et al.* 2015; Revil *et al.* 2015).

Finally, the Cole-Cole exponent c_P decreases as f_C increases (Fig. 4c). This indicates that the macroscopic parameter c_P differs from c, the microscopic (or local) value set at 0.8 in our simulations. This finding is consistent with the results reported by Maineult *et al.* (2017), where c_p decreases with the increase of the heterogeneity of the radius distribution (see their figs 3 and 4). In this context, increasing the fraction of capacitors effectively increases the heterogeneity of the medium. The presence of the capacitors affects the parallel (vertical) current flow in the network. Both inhomogeneous radius distribution and the presence of capacitors cause a distortion of the uniform current flow through the network.

4 APPLICATION TO DATA

4.1. Monomodal sand-pyrite-water mixtures

4.1.1 Data set and Pelton parameters

We simulate the SIP response of sand-pyrite-water mixtures as reported by Hupfer *et al.* (2016) and Martin & Weller (2023). We refer to as monomodal samples those with a pyrite fraction with only one fixed grain size. A total of twelve spectra of monomodal samples are available (Fig. 5), corresponding to different pyrite contents in the solid fraction p_{vs} (ranging from 0.5 to 6 per cent), and varying pyrite grain sizes (Table 1). After removing the high frequency trends from the data (see Appendix), we fitted the spectra using the Pelton model (eq. 7). Overall, there is a good agreement between the measured spectra and their corresponding Pelton model fits. The determined Pelton parameters are summarized in Table 2.

4.1.2 Determination of f_C, R, C and c

For each sample, we determine the fraction of capacitors f_C (which differs from the volume fraction of pyrite grains in the solid phase p_{vs}), the resistance R of the passive links, as well as the capacitance C and exponent c of the active links. We used $15 \times 15 \times 15$ networks (3375 nodes, 9 450 links) with a characteristic cell size L set to the mean diameter of the sand grains. The procedure can be summarized as follows:

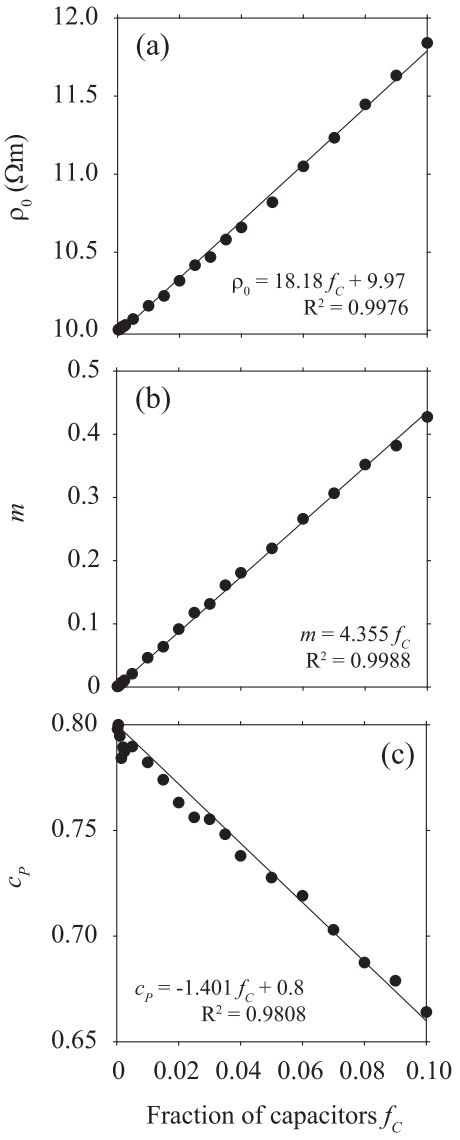

Figure 4. Effect of the fraction of capacitors f_C on the Pelton parameters: DC resistivity ρ_0 (a), chargeability m (b) and Cole-Cole exponent c_P (c).

(1) Generation of a random network with a fraction of capacitors f_C randomly selected within a predefined interval;
(2) Determination of the resistance R needed to match the amplitude of the given spectrum at both zero and infinite frequencies;
(3) Determination of the capacitance C and exponent c values that best explain the amplitude and phase spectra across the entire frequency range.

Regarding step (2), it is important to note that at zero frequency, the impedance of the capacitors is infinite, whereas at infinite frequency, it approaches zero. Thus, when analysing the system at these two frequency limits, only one parameter, the resistance R, needs to be determined. Consequently, using the system at zero and infinite frequencies, we identify the optimal R value required to match ρ_0 and ρ_∞ by applying the simplex method and the cost-function F_R:

$$F_R = \max\left(\left|\rho_0^{\text{observed}} - \rho_0^{\text{predicted}}\right|, \left|\rho_\infty^{\text{observed}} - \rho_\infty^{\text{predicted}}\right|\right). \quad (9)$$

Using the trial-and-error method, we found that when F_R exceeded 0.05 Ωm, the selected fraction of capacitors was not optimal. In such cases, the procedure stopped before step (3) and returned to step (1). Otherwise, the process continued. Once R was determined, we applied the simplex method again to optimize $\log_{10}(C)$ and c, using the cost-function F from eq. (8). The procedure was repeated until a statistically sufficient number of models (i.e. 50) satisfied the condition $F < 0.0035$ (0.0045 for C05 and 0.0055 for D05).

The optimization results for sample E02 are presented in Fig. 6, showing a well-constrained parameter estimation, with a bell shape distributions and narrow variation ranges. The plots in Fig. 7 indicate that most parameter pairs are weakly correlated, except for $\log_{10}(C)$ and c, which exhibit a stronger relationship. The mean parameter values for the entire data set are summarized in Table 3. Finally, Fig. 8 confirms a good agreement between the measured and fitted spectra, comparable to the fitting quality achieved with the Pelton model in Fig. 5.

4.1.3 Discussion of the results concerning monomodal samples

A power-law relationship between the radius of pyrite grains r and the time constant of the Pelton model τ_P has been reported in many experimental studies on sand-pyrite mixtures. Using the data displayed in Fig. 9(a), we determine a power-law exponent of 1.706.

The networks consisting of electrical elements (resistors and capacitors) do not consider the radius of the pyrite grains. The pore radius r is not an intrinsic parameter of network modelling. However, the resulting optimized parameters (f_C, R, C) indicate a dependence on r as demonstrated in Figs 9(b)–(d). The fraction of capacitors f_C does not exactly match the pyrite content in the solid fraction, as shown in Fig. 9(b). Specifically, we observe a slight decrease in f_C with increasing pyrite grain radius. This trend may be explained by the fact that, for a given pyrite volume in the solid fraction, the number of particles N increases as their size decreases. However, the increase of the number N follows a power law ($N \sim 1/r^3$) that would overestimate the observed increase in f_C. Up to now, the electrical networks cannot correctly represent the volume ratios between sand grains, pore channels and pyrite particles. Nevertheless, we found an empirical relationship between f_C and p_{vs} multiplied by a correction factor that depends on the ratio r/r_s:

$$f_C = p_{vs}\left(\frac{r}{r_s}\right)^{\alpha} \quad (10)$$

with r_s is the radius of sand grain, and an exponent α equal to -0.22 that has been determined by optimization. Eq. (10) indicates that f_C approaches p_{vs} for $r >> r_s$. The graph in Fig. 10 compares the value of f_C resulting from network modelling with the prediction of eq. (10) that uses exclusively parameters characterizing the sand-pyrite-water mixture.

The increase in R with r for samples E (Fig. 9c) corresponds to the increase of the resistivity ρ_0 shown in Table 2. This increase is attributed to a change in water resistivity after sample preparation. Although, all samples have been saturated with the same NaCl-brine of ~ 0.1 Ωm, the chemical reaction of pyrite with water and

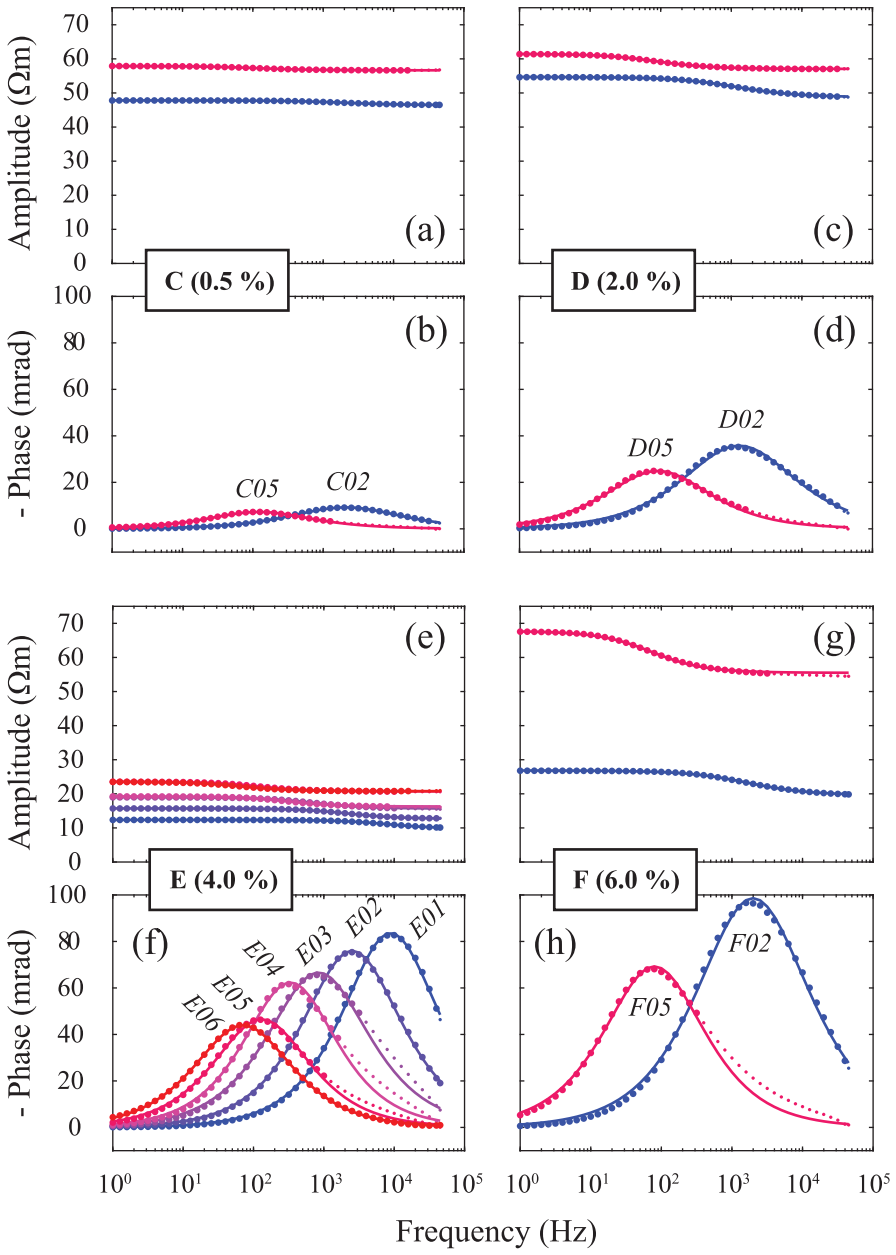

Figure 5. Experimental data (dots) and Pelton model fitting (lines) for the monomodal samples (a, c, e, g: resistivity amplitude; b, d, f, h: phase). Red shades indicate the largest grain radii, while blue shades correspond to the smallest ones. Note that data points marked with small dots were excluded from the fitting process. See Table 1 for details.

air during sample preparation caused a decrease in fluid resistivity shortly after sample preparation. The decrease became stronger for the samples with smaller grain size because of their larger surface area that contributes to the chemical reactions (Martin & Weller 2023).

The strong relationship between capacitance C and r (Fig. 9d) suggests that C is the most relevant parameter of the electrical network that enables a simulation of a change in r (see section 5.2).

Regarding resistivity, Fig. 11 shows a perfect match between the mean values of R multiplied by the unit length $L = 2\ r_S$ and the quantity $\rho_{S\&W} = 3/(2/\rho_0 + 1/\rho_\infty)$. This latter expression corresponds to the frequency-independent resistivity of the background sand–water mixture without pyrite grains, as described by Revil *et al.* (2015). We find that R depends only on ρ_0 and ρ_∞. Therefore, the determination of R by optimization can be omitted.

As observed in the numerical simulations (see Section 3), chargeability increases linearly with f_C (Fig. 12a), with a slope very close to the reported value of 9/2 (Revil *et al.* 2015). Assuming that the fraction of capacitors f_C reflects somehow the volume fraction of metallic particles in the medium, the consistency in the slope suggests that network modelling and mixing laws reflect similar relationships. Regarding the exponents, Fig. 12(b) confirms that c_P is always smaller

Table 1. Characteristics of the monomodal sand-pyrite-water mixtures. Samples C, D and F from Hupfer *et al.* (2016); Samples E from Martin & Weller (2023).

Sample	Pyrite content in solid fraction p_{vs} (vol. per cent)	Pyrite grain radius range (μm)	Mean pyrite grain radius r (μm) ∗	Mean sand grain radius r_s (μm) ∗
C02	0.5	56–100	75	78
C05	0.5	315–500	397	78
D02	2	56–100	75	78
D05	2	315–500	397	78
E01	4	31–56	42	100
E02	4	56–100	75	100
E03	4	100–178	133	100
E04	4	178–315	236	100
E05	4	315–500	397	100
E06	4	500–1000	707	100
F02	6	56–100	75	78
F05	6	315–500	397	78

∗ Geometric mean.

Table 2. Determined Pelton parameters for the monomodal samples.

Sample	ρ_0 (Ωm)	m	τ_P (s)	c_P	$\rho_\infty = (1-m)\rho_0$
C02	47.8	0.029	$7.74\ 10^{-5}$	0.709	46.4
C05	57.9	0.022	$1.32\ 10^{-3}$	0.747	56.6
D02	54.7	0.109	$1.34\ 10^{-4}$	0.706	48.7
D05	61.5	0.072	$1.83\ 10^{-3}$	0.746	57.0
E01	12.4	0.207	$2.06\ 10^{-5}$	0.798	9.80
E02	15.7	0.195	$7.24\ 10^{-5}$	0.781	12.7
E03	19.0	0.176	$2.16\ 10^{-4}$	0.767	15.6
E04	19.3	0.154	$5.30\ 10^{-4}$	0.817	16.3
E05	23.6	0.121	$1.33\ 10^{-3}$	0.795	20.7
E06	23.5	0.117	$2.42\ 10^{-3}$	0.784	20.8
F02	26.9	0.270	$9.97\ 10^{-5}$	0.715	19.6
F05	67.8	0.181	$2.28\ 10^{-3}$	0.771	55.5

than c, and Fig. 12(c) shows that the ratio c_P/c decreases as f_C increases.

We relate the mean values of the optimized parameters R, C and c to the Pelton time constant τ_P. Our 3-D network simulations yield:

$$\tau_P = C\left(\frac{R}{2}\right)^{1/c}, \tag{11}$$

with an excellent agreement, as demonstrated in Fig. 13.

Eq. (11) also explains the correlation observed between c and $\log_{10}(C)$ in Fig. 7(f). Rearranging eq. (11), we obtain:

$$c = \frac{\log_{10}\frac{R}{2}}{\log_{10}\tau_P - \log_{10}C}. \tag{12}$$

The curve in Fig. 7(f) corresponds to the equation:

$$c = \frac{\log_{10}\frac{\langle R\rangle}{2}}{\log_{10}\tau_P - \log_{10}C}, \tag{13}$$

where $< R >$ is the mean value of the resistances determined during the optimization for the considered sample (see column 2 of Table 3). This equation is in good agreement with the observed correlation between c and $\log_{10}(C)$. Obviously, small changes in c can be compensated by changes in C without any loss in fitting quality.

4.2. Bimodal sand-pyrite-water mixture

As a next step, we applied our methodology to the data set reported by Martin & Weller (2023) for the superposition of two monomodal sand-pyrite-water mixtures. The mixtures of two monomodal mixtures are referred to as bimodal mixtures. The bimodal Z samples contain 4 per cent of pyrite in the solid fraction with radius r_1, and 4 per cent of pyrite in the solid fraction with radius r_2 (Table 4). After removing the high-frequency trend (see Appendix), we fitted the spectra using a double Pelton model:

$$\rho_P^* = \rho_0\left(1 - m_1\left(1 - \frac{1}{1+(i\omega\tau_{P,1})^{c_{P,1}}}\right) - m_2\left(1 - \frac{1}{1+(i\omega\tau_{P,2})^{c_{P,2}}}\right)\right), \tag{14}$$

with the constraint that the chargeability m_2 and the Cole-Cole exponent $c_{P,2}$, associated to the content of pyrite grains of radius r_2, were the same for the five samples (Figs 14a and b and Table 5).

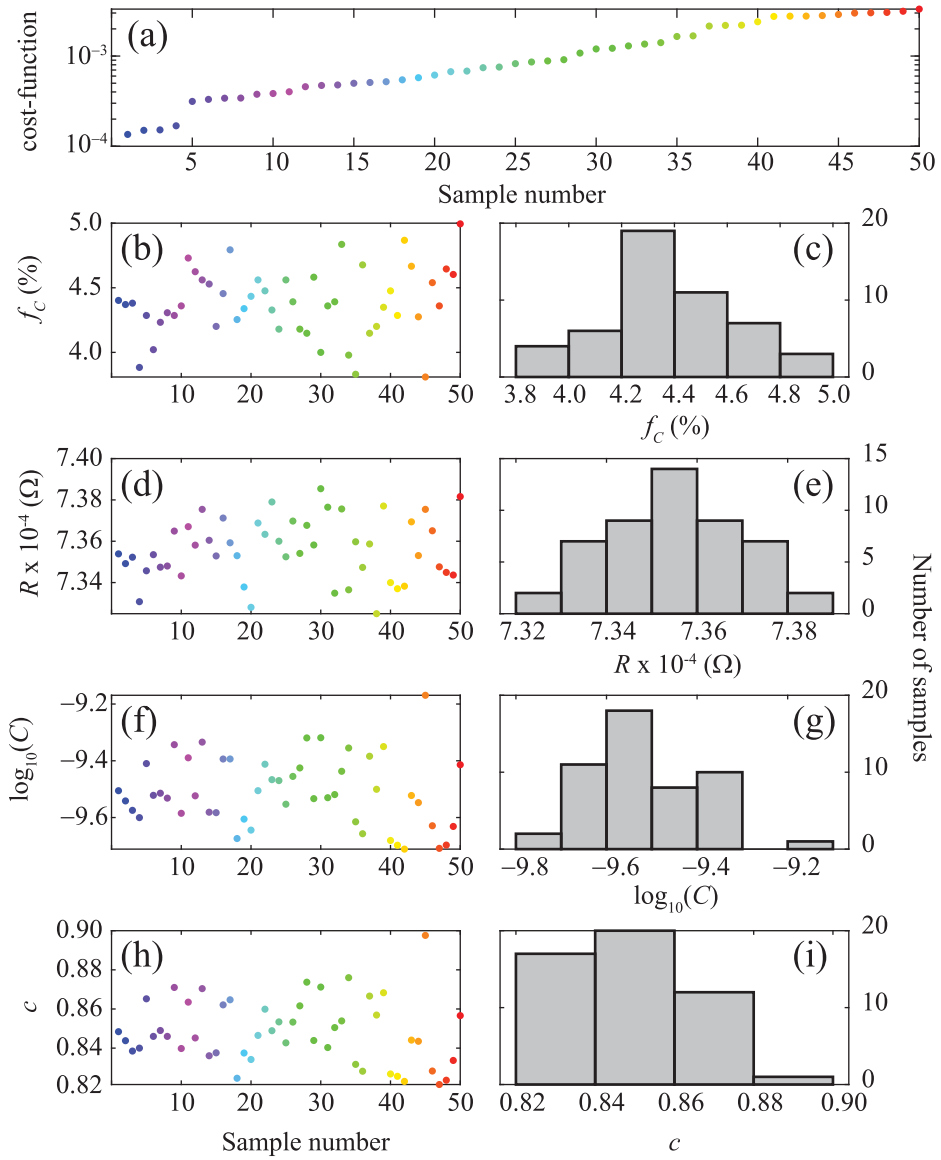

Figure 6. Optimization results for sample E02: sorted cost-function values for the 50 best models (a), values of the optimized parameters f_C, R, $\log_{10}(C)$ and c (b, d, f,h) and associated distributions (c, e, g, i).

Our methodology of network modelling does not allow to determine $f_{C,1}$ and $f_{C,2}$ separately, but $f_{C,1} + f_{C,2}$ only. That is the reason why we decided to fix $f_{C,1}$ and $f_{C,2}$, using the experimental relationship determined for the E samples ($p_{vs} = 4$ per cent), that is, $f_C = -1.838 \log_{10}(r) - 3.290$ (Fig. 9b). We estimated the parameters R, C_1, C_2, c_1 and c_2 using $12 \times 12 \times 12$ networks (1728 nodes, 4752 links). Once again, the simulated spectra show excellent agreement with the experimental data (Figs 14c and d). The mean values of the optimized parameters, computed over the best 10 models, are summarized in Table 6.

We observe again a good agreement of τ_P with the results eq. (11) using the parameters determined for the two fractions of pyrite particles. Fig. 15 adds to the graph in Fig. 13 the data points for the bimodal samples that are located close to the diagonal line representing eq. (11). Note that the spectra of sample Z05 with a continuous distribution of the pyrite radii from 315 to 1000 μm can be fitted by the original Pelton model (eq. 7), and optimized as a monomodal sample. The resulting parameters τ_P and $C(R/2)^{1/c}$ are displayed by a black circle in Fig. 15 that is located at the diagonal line.

5 DISCUSSION

5.1. Comparison with Pelton model

As explained in Section 2.4, the Pelton model considers two pores in parallel, one fluid filled pore having a resistance R_0, and one blocked by a pyrite grain, having an impedance $R_1 + (i\omega C_p)^{c_P}$. The time constant of this simple circuit is given by:

$$\tau_P = C_P \left(\frac{R_0}{m_P} \right)^{1/c_P}, \tag{15}$$

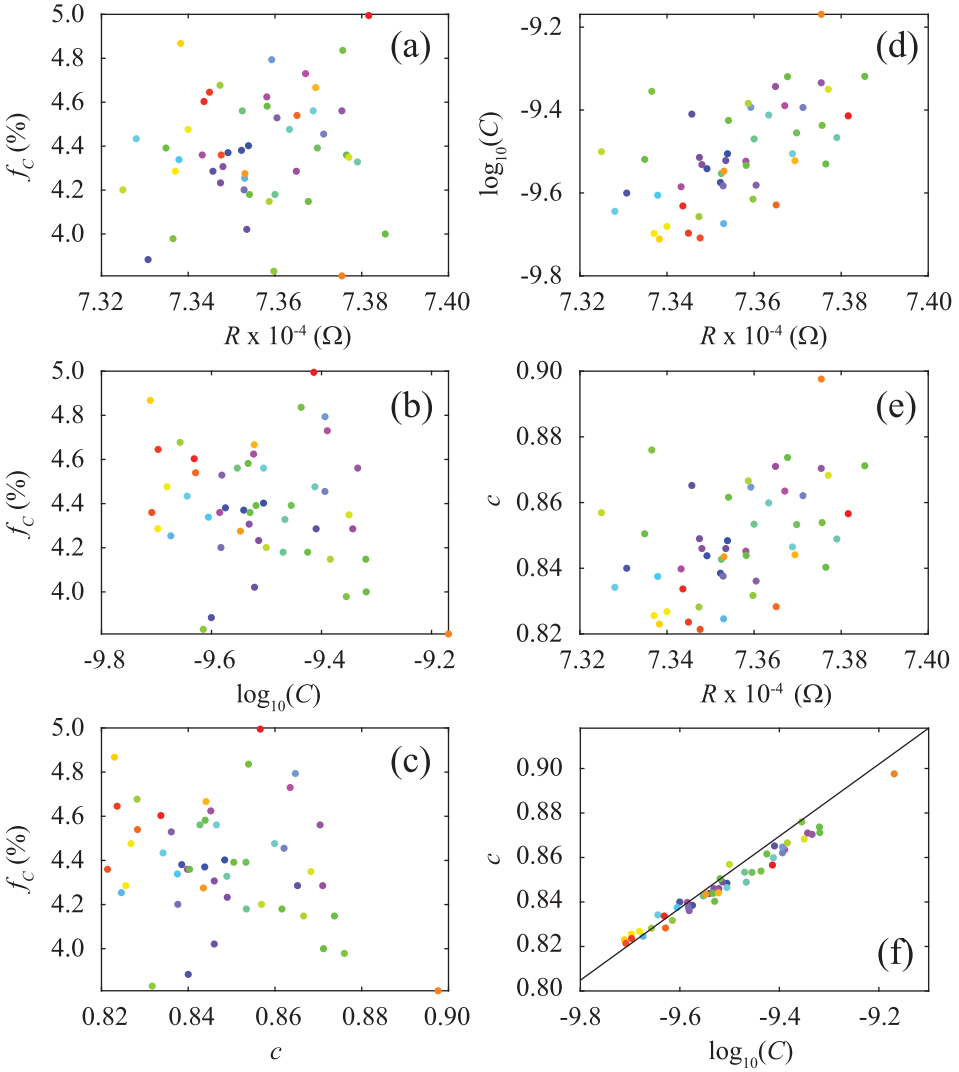

Figure 7. Correlations between the optimized parameters f_C, R, $\log_{10}(C)$ and c for Sample E02. Only c and $\log_{10}(C)$ are correlated (f). The solid line in (f) corresponds to the prediction of eq. (13).

Table 3. Optimized parameters for the monomodal samples.

Sample	$< f_C >$ (per cent)	$<R>$ (Ω)	$<\log_{10}(C)>$	$<c>$
C02	0.686	303 153	−11.199	0.729
C05	0.487	367 909	−9.757	0.766
D02	2.416	337 380	−10.911	0.742
D05	1.633	384 204	−9.523	0.777
E01	4.611	57 545	−9.809	0.869
E02	4.383	73 560	−9.509	0.848
E03	3.966	89 436	−9.279	0.828
E04	3.493	91 451	−8.604	0.874
E05	2.695	113 306	−8.464	0.848
E06	2.567	113 203	−8.344	0.828
F02	6.134	155 964	−10.125	0.798
F05	4.067	407 403	−9.018	0.832

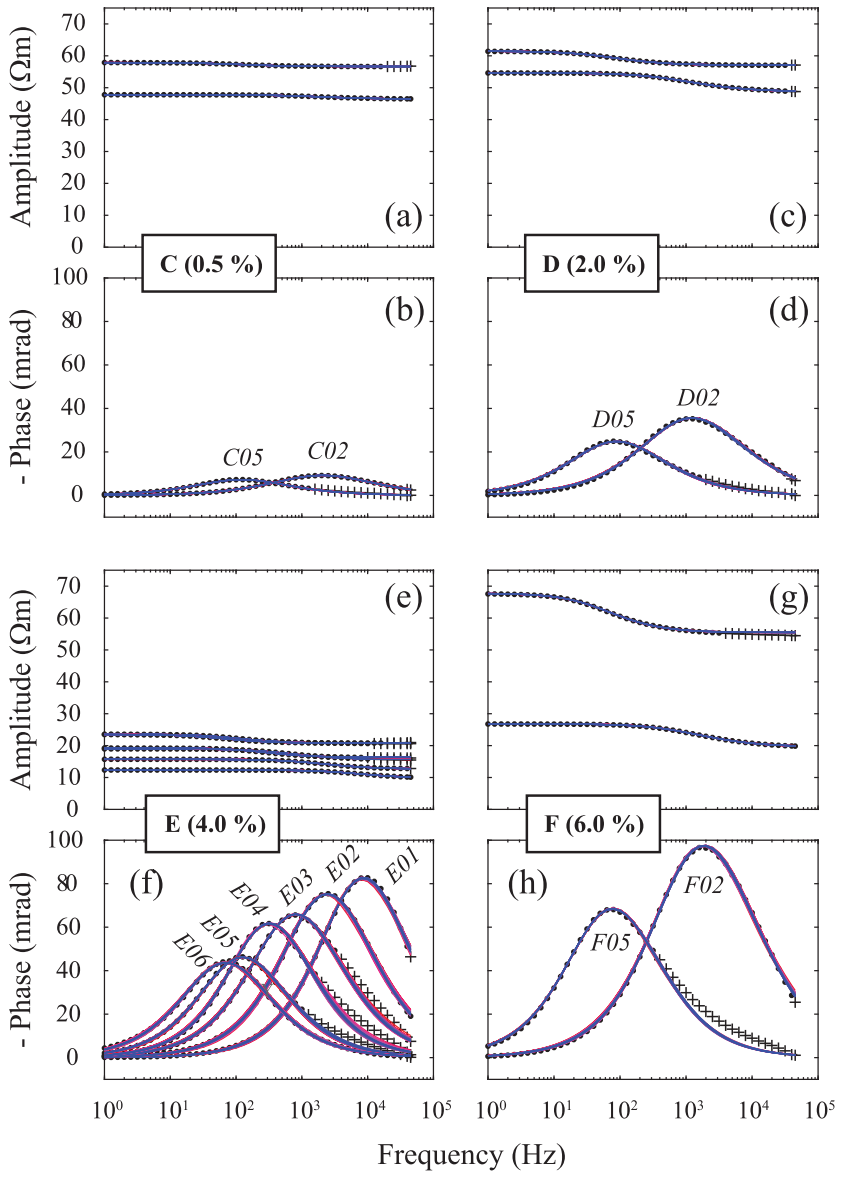

Figure 8. Comparison of measured and modelled resistivity spectra for the monomodal samples (a, c, e, g: resistivity amplitude; b, d, f, h: phase). For each sample, the 50 best models are shown (the purple colour corresponds to the model with the largest cost-function value, the blue colour to the model with the smallest cost-function value). Dots represent experimental data, while crosses indicate data points excluded from the cost-function computation. 15 × 15 × 15 networks were used.

where m_P is the chargeability equal to $R_0/(R_0 + R_1)$. Considering eq. (11), we find that our networks are equivalent to Pelton circuits with $R_1 = 0$ and $R_0 = R/2$. Moreover, we observe in Fig. 12a that f_C is proportional to m. Eq. (11) indicates that the time constant τ_P only depends on the network parameters R, C, and c. Therefore, m and consequently f_C has no influence on τ_P. This is a remarkable difference to eq. (15) that shows that in the Pelton model the time constant τ_P depends on all other parameters R_0, m_P, C_P, and c_P. We find that our network approach decouples the influence of the properties of the individual links (R for the passive links, C and c for the active links, which controls the time constant) and the influence of the number of active links (i.e. f_C, which controls the chargeability m). The decoupling becomes evident by the absence of correlation between f_C at the one side and R, C and c on the other side as shown in Figs 7(a)–(c).

5.2 Effect of the unit cell length L

The selection of the unit cell length L is a non-trivial decision. In this study, we define L as the mean diameter of the sand grains. To investigate the impact of this choice, we examine the effects of varying L. Let us consider a different length $L'=nL$ (with n being an arbitrary factor $\neq 1$), and determine the values C' and R' associated to L'.

From Fig. 11, we can suppose that:

$$R' = \frac{\rho_{S\&W}}{L'} = \frac{\rho_{S\&W}}{nL} = \frac{R}{n}. \tag{16}$$

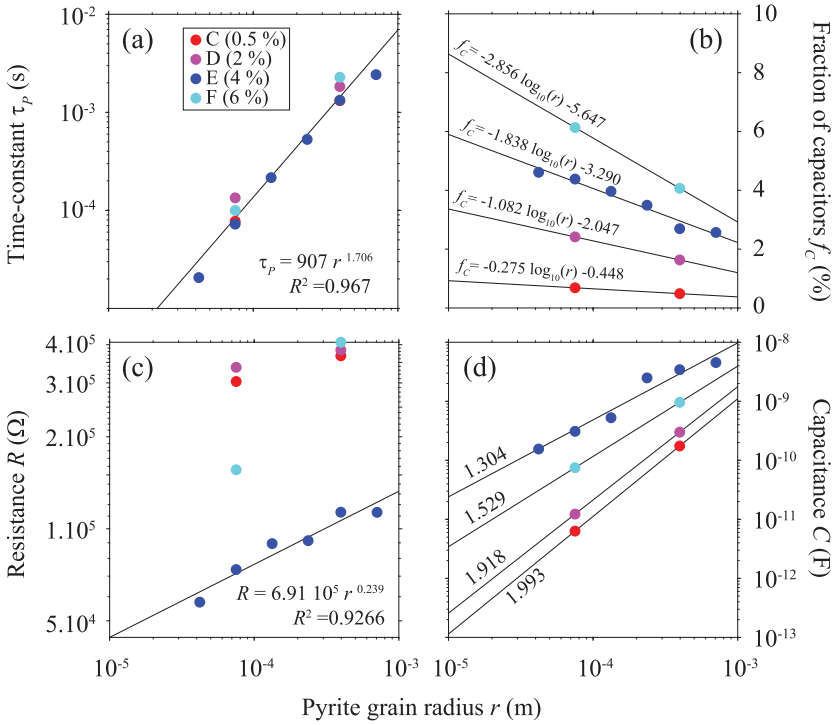

Figure 9. Time-constant τ_P (a), fraction of capacitors f_C (b), resistance R (c), capacitance C (d) as a functions of pyrite grain radius. The numbers in (d) indicate the exponent of the power law.

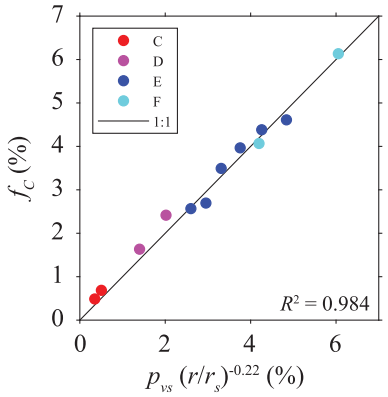

Figure 10. Comparison of the fraction of capacitors f_C with the prediction of eq. (10) using the pyrite content in the solid fraction p_{vs} and the ratio between pyrite and sand grain radius r/r_s.

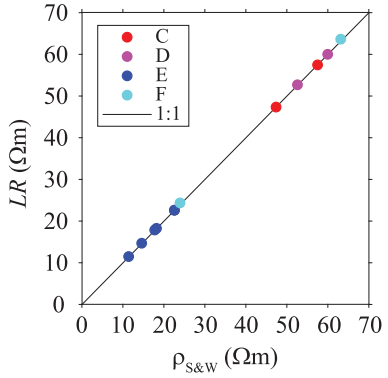

Figure 11. Relationship between LR and $\rho_{S\&W} = 3/(2/\rho_0 + 1/\rho_\infty)$.

Moreover, the time constant τ_P (associated to the peak of the phase) should not change, as well as the value of c (associated to the width of the phase curve), so we can write (from eq. 11):

$$\tau_P = C\left(\frac{R}{2}\right)^{1/c} = C'\left(\frac{R'}{2}\right)^{1/c} = C'\left(\frac{\rho_{S\&W}}{2nL}\right)^{1/c} = C'\frac{1}{n^{1/c}}\left(\frac{\rho_{S\&W}}{2L}\right)^{1/c}$$

$$= C'\frac{1}{n^{1/c}}\left(\frac{R}{2}\right)^{1/c}. \quad (17)$$

It follows that:

$$C' = Cn^{1/c} \quad (18)$$

To verify the validity of eqs (16) and (18) and the assumptions behind, we applied our methodology to sample E02, using L'=2 L. In this case, we obtained a value for f_c equal to 4.37 per cent (similar to 4.24 per cent, the value determined using $L = 2r_s$) and a c value of 0.849 (close to 0.848). We obtained R'=36 748 Ohm (close to $R/2$ = 36 774 Ohm), and C'=6.94 10^{-10} F (close to $C2^{1/c}$ = 6.91 10^{-10} F). As a consequence, changing L will change R and C, but not the time constant, and neither the fraction of capacitors nor the Cole-Cole exponent c.

5.3. About the significance of f_C

The numerical network modelling has shown that 3-D networks are able to reproduce the complex resistivity spectra of the monomodal and bimodal samples. Considering the proportionality between f_C and m in Fig. 11(a), we find that m is related to the volume percentage of metallic particles as predicted by the effective medium

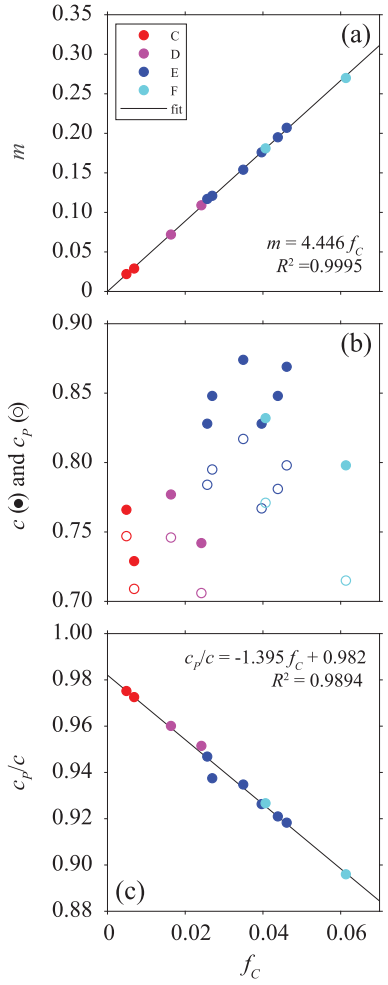

Figure 12. Pelton chargeability m (a), optimized exponent c and Cole-Cole exponent c_P (b) and ratio c_P/c (c) as function of the fraction of capacitors f_C.

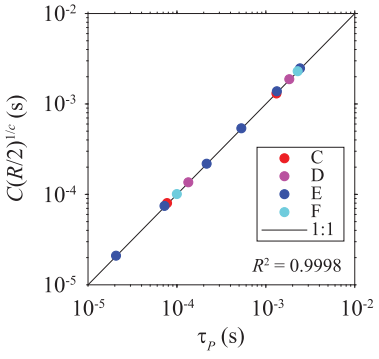

Figure 13. Quantity $C(R/2)^{1/c}$ as function of the Pelton time constant τ_P for the monomodal samples.

theory (e.g. Gurin *et al.* 2015; Revil *et al.* 2015). However, beside the volume percentage of metallic particles, the particle size has a non-vanishing effect on the chargeability m. This effect has already been reported for the experimental results in Martin & Weller (2023). The additional grain-size effect may originate from the interaction of metallic particles in the electrical field that is ignored both in the effective medium theory and in the electrochemical models that consider only a single particle (Wong 1979; Bücker *et al.* 2018). The network model ignores in a similar way the interaction between neighbouring capacitors. This is another reason that f_C cannot correctly reflect the volume percentage of metallic particles. However, f_C can be related to pyrite content expressed by its fraction in the solid volume p_{vs} considering the ratio r/r_s (Fig. 10 and eq. 10).

5.4. About the dependence of the microscopic parameters on pyrite grain radius

The resistance R depends weakly on the pyrite grain radius r (Fig. 9c). The reason has already been discussed in Section 4.1.3. However, C depends strongly on r. Regarding Fig. 9(d), we cannot exclude any influence of the fluid resistivity on the capacitance due to electrochemical reactions at the surface of the pyrite grains for instance. To remove the influence of R, we define a corrected capacitance:

$$C_{\text{corr}} = \tau_P \left(\frac{R_m}{2}\right)^{-1/c_m}, \tag{19}$$

where R_m and c_m are the mean values of $< R >$ and $< c >$ computed over the whole set of monomodal samples (Table 3), respectively.

The relationship between C_{corr} and r, which is displayed in Fig. 16, shows a strong correlation. The power law between C_{corr} and r indicates an exponent of 1.706 that corresponds exactly to the exponent of the power law between τ_P and r as shown in Fig. 9(a).

The value of the exponent is higher than the theoretical value of 1 for spherical condensers (see e.g. Feng *et al.* 2020). The higher value of the exponent may be attributed to the deviation from a spherical shape and to the rough surface of the pyrite particles. Regarding the existing power law relationship, it seems possible to determine the radius of the pyrite grains from the corrected capacity:

$$r = \alpha C_{\text{corr}}{}^{\beta}. \tag{20}$$

Using the data in Fig. 16, we determined $\alpha = 77.6$ and $\beta = 0.59$ with C given in F and r in metre.

5.5. Is a 3-D approach necessary?

The question arise whether a 3-D approach is necessary. Do impedances perpendicular to the electrical potential gradient significantly influence the complex resistivity spectra of the investigated network? To address this, we generate two random networks, with 5 per cent and 10 per cent capacitors respectively, and computed their responses (blue lines in Fig. 17). We then replaced the capacitors orientated along the *i*- and *j*- directions (see Fig. 1) with resistors and recomputed the spectra (red lines in Fig. 17). By comparing the two sets of spectra, it becomes

Table 4. Characteristics of the bimodal sand-pyrite-water mixtures [Martin & Weller (2023)].

Sample	Mean pyrite grain radius r_1 (μm) ∗	Mean pyrite grain radius r_2 (μm) ∗	$p_{vs,1}$ (per cent)	$p_{vs,2}$ (per cent)	Mean sand grain radius r_s (μm) ∗
Z01	42	707	4	4	100
Z02	75	707	4	4	100
Z03	133	707	4	4	100
Z04	236	707	4	4	100
Z05	397	707	4	4	100

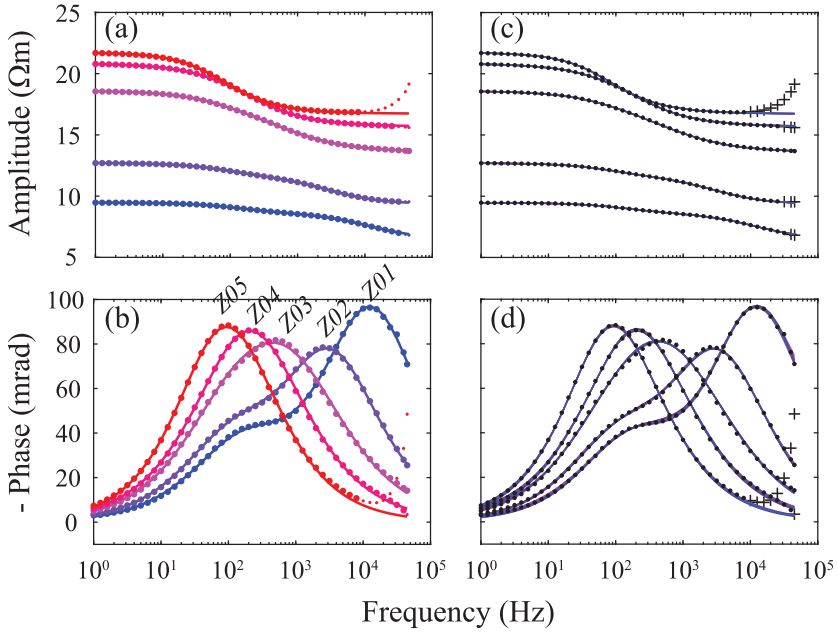

Figure 14. Complex resistivity spectra resulting from double Pelton model fitting (a, b) and optimization with network modelling (c, d) for the bimodal Z samples. In (c) and (d), 12 × 12 × 12 networks were used, and the 10 best models are shown for each sample. The purple shade corresponds to the model with the largest cost-function value, the blue shade to the model with the smallest cost-function value.

Table 5. Determined double Pelton parameters for the bimodal Z samples.

Sample	ρ_0 (Ωm)	m_1	τ_{P1} (s)	c_{P1}	m_2	τ_{P2} (s)	c_{P2}	ρ_∞ (Ωm)	m_{tot}
Z01	9.48	0.219	$1.44\ 10^{-5}$	0.754	0.096	$1.13\ 10^{-3}$	0.731	6.49	0.315
Z02	12.7	0.171	$5.40\ 10^{-5}$	0.754	0.096	$1.60\ 10^{-3}$	0.731	9.32	0.267
Z03	18.6	0.173	$2.34\ 10^{-4}$	0.664	0.096	$1.72\ 10^{-3}$	0.731	13.6	0.269
Z04	20.9	0.152	$8.47\ 10^{-4}$	0.672	0.096	$1.06\ 10^{-3}$	0.731	15.7	0.248
Z05	21.8	0.135	$2.63\ 10^{-3}$	0.807	0.096	$1.11\ 10^{-3}$	0.731	16.7	0.231

Table 6. Fixed (f_C) and optimized parameters (R, C and c) for the bimodal Z samples.

Sample	$<f_{C,1}>$ (per cent)	$<f_{C,2}>$ (per cent)	$<R>$ (Ω)	$\log_{10}(C_1)$	$\log_{10}(C_2)$	$<c_1>$	$<c_2>$
Z01	4.756	2.504	42 366	−9.759	−8.666	0.873	0.769
Z02	4.293	2.504	57 728	−9.530	−8.507	0.842	0.789
Z03	3.830	2.504	84 491	−9.785	−9.199	0.735	0.755
Z04	3.367	2.504	95 511	−10.047	−8.161	0.664	0.919
Z05	2.946	2.504	100 298	−9.429	−7.573	0.702	0.969

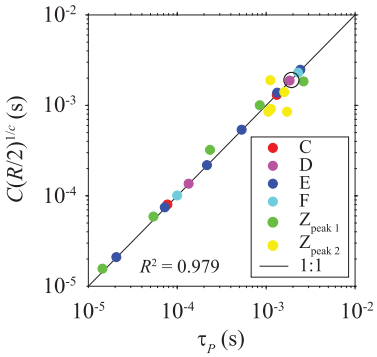

Figure 15. Quantity $C(R/2)^{1/c}$ as a function of the Pelton time constant τ_P for all samples. The black circle corresponds to sample Z05 considered as a monomodal sample.

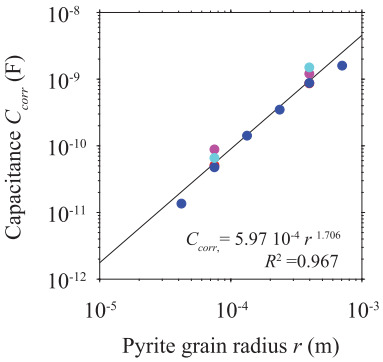

Figure 16. Corrected capacitance as a function of pyrite grain radius for the monomodal samples.

evident that perpendicularly orientated capacitors do have an effect, particularly at frequencies above the phase peak. This suggest that electrical currents also pass through these perpendicular capacitors. Consequently, we conclude that a 3-D approach is necessary.

5.6. On the influence of the network realization

We examine the influence of network realizations. Since each network is generated randomly, the computed spectra may exhibit slight variations from one realization to another. To quantify the magnitude of these differences, we generated 25 30 × 30 × 30 networks with identical characteristics in terms of f_C, R, C and c. However, the spatial distribution of the active links in the network changes. Fig. 18 displays the variation for the different realizations. The results show that the maximum deviation between the resistivity amplitude and the mean amplitude across the 25 spectra does not exceed 0.5 per cent. For the phase, the variation remains below 4 mrad (for a maximum phase of 65 mrad), which is within an acceptable range. This finding highlights the importance of using a sufficient number of realizations to obtain reliable mean values for the model parameters.

5.7. Limitations of the approach

Theoretically, the fraction of active links in a network can reach up to 100 per cent. The simulation of the response of larger fractions of polarizing particles seems to be an advantage of network modelling compared to the effective medium theory that is only valid for small additions of metallic particles into a mixture. However, similarly to electrochemical models or models derived from the effective medium theory, network modelling is not able to consider the interaction between neighbouring polarizing elements. We have learnt from the experimental results that even for a small amount of pyrite particles (e.g. $p_{vs} = 4$ per cent) the rising number of particles per volume causes an increase in chargeability that might be caused by the interaction of particles.

The effect of the interaction of particles can only be investigated by numerical modelling at the grain scale (e.g. Kreith et al. 2024). A further step would be the integration of the results of small-scale modelling into the network modelling approach (e.g. by modifying the impedance expressions to take into account the possible interactions).

In addition, the network used in our study is quite ‘rigid’, with a fixed cubic mesh (coordination number of 6), and identical geometrical characteristics for the pores. Further works should include the use of unstructured meshes allowing the pores to vary in length, radius and orientation. A higher coordination number would be necessary to enable the investigation of anisotropy by network modelling.

6 CONCLUSIONS

Using 3-D networks of impedances represented by resistors or leaky capacitors, we successfully reproduced the complex resistivity spectra of sand-pyrite-water mixtures reported by Hupfer *et al.* (2016) and Martin & Weller (2023). Water saturated pores were modelled as resistors with resistance R, while pyrite grains were represented by leaky capacitors with an impedance $Z_c = (i\omega C)^{-c}$. We found that chargeability is approximately 9/2 times the fraction of links associated with pyrite grains, in agreement

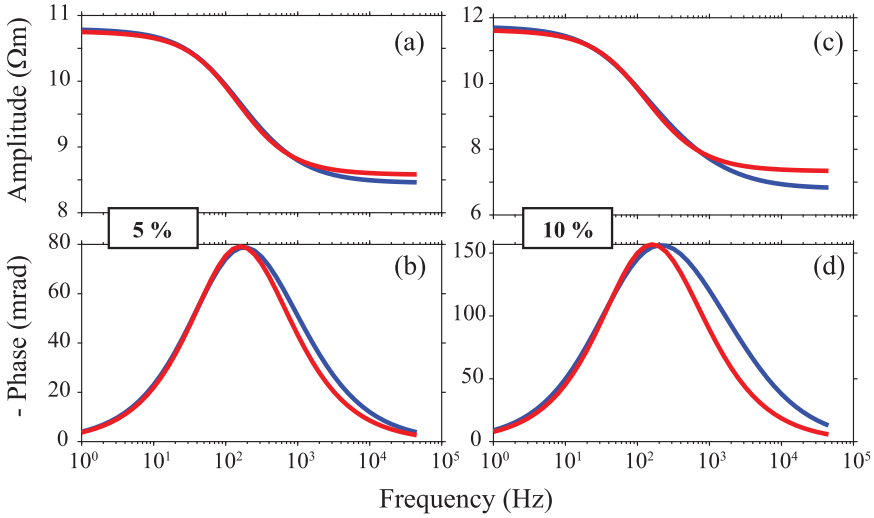

Figure 17. 3-D effects on a 30 × 30 × 30 network with 5 per cent and 10 per cent capacitors (a, c: amplitude; b, d: phase). Blue lines represent the response of the full network, while red lines correspond to network where capacitors perpendicular to potential gradient direction have been replaced by resistors ($R = 50\,000\ \Omega$, $C = 10^{-8.5}$ F, $c = 0.8$, $L = 200\ \mu$m).

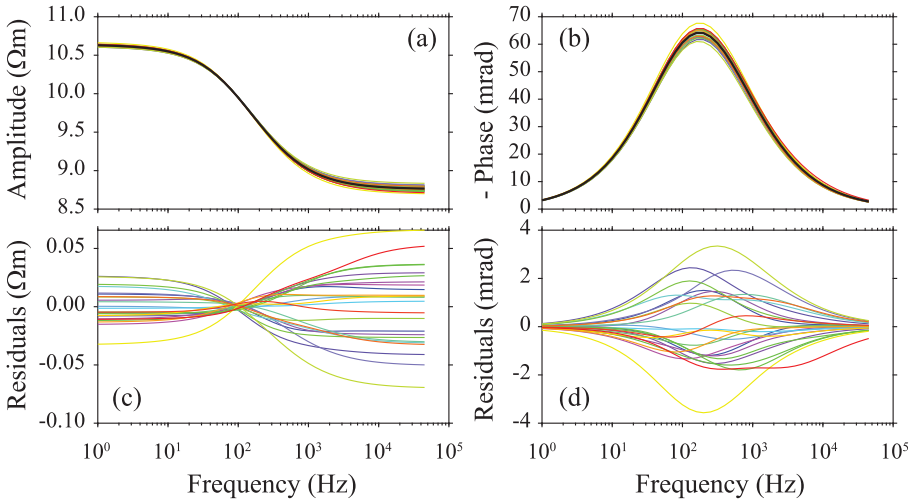

Figure 18. Influence of the network realization on resistivity amplitude (a) and phase (b), with differences between individual spectra and average spectrum (c and d). Results are based on 25 simulations of 30 × 30 × 30 networks with 4 per cent capacitors ($R = 50\,000\ \Omega$, $C = 10^{-8.5}$ F, $c = 0.8$, $L = 200\ \mu$m). The black line represents the average spectrum (arithmetic mean).

with models derived from the effective medium theory. However, the fraction of capacitors does not exactly correspond to the volume fraction of pyrite grains in the solid phase of the sand-pyrite-water mixtures.

The Pelton time constant is related to the parameters of the network elements by $\tau_P = C(R/2)^{1/c}$ and it was found to be proportional to the pyrite grain radius raised to the power of 1.7. Our network modelling experiments also revealed that the microscopic exponent c is consistently larger than the macroscopic Cole-Cole exponent obtained from Pelton fitting. By comparing 3-D network modelling with the phenomenological Pelton model, we demonstrated that the sample-scale parameters are closely linked to the underlying pore and grain size characteristics.

The methodology reported here, coherent with the classical model of Pelton *et al.* (1978), could be useful to study the effect of the spatial distribution of the ore grains, or mixing of different ore types, in a more realistic way. However, the network modelling does not take into account the interaction between neighbouring polarizing particles. Therefore, the results become questionable if the interaction of particles cannot be ignored.

Further works should include a combination of different networks to simulate larger volumes with a more complicated distribution of polarizing particles. The methodology reported here, which enables us to examine the effects of scale variation (i.e. from pore to sample scale) on the SIP response, is quite general, and could be applied to a variety of other polarizing material, such as mixtures with semiconductors, clays or organic matter.

ACKNOWLEDGMENTS

The authors sincerely thanks the two reviewers and the Editor, Dr Line Meldgaard Madsen, for their questions and comments that helped us to finalize the manuscript. KT acknowledges the support of the Russian Science Foundation through the grant № 25–27-00360 'Investigation of natural and anthropogenic Earth electrical field as a source of power generation'.

DATA AVAILABILITY

Data used in this study are published in Hupfer *et al.* (2016) and Martin & Weller (2023).

REFERENCES

Abdulsamad, F., Florsch, N. & Camerlynck, C. 2017. Spectral induced polarization in a sandy medium containing semiconductor materials: experimental results and numerical modelling of the polarization mechanism, *Near Surf. Geophys.,* **15,** 669–683.

Binley, A. & Slater, L., 2020. *Resistivity and Induced Polarization: Theory and Applications to the Near-Surface Earth*. Cambridge Univ. Press.

Bücker, M., Flores-Orozco, A. & Kemna, A., 2018. Electrochemical polarization around metallic particles—part 1: the role of diffuse-layer and volume-diffusion relaxation, *Geophysics,* **83,** E203–E217.

Cole, K.S. & Cole, R.H., 1941. Dispersion and absorption in dielectrics, *J. Chem. Phys.,* **9,** 341.

Dias, C.A., 2000. Developments in a model to describe low-frequency electrical polarization of rocks, *Geophysics,* **65,** 437–451.

Feng, L., Li, Q., Cameron, S.D., He, K., Colby, R., Walker, K.M., Deckman, H.W. & Ertas, D., 2020. Quantifying induced polarization of conductive inclusions in porous media and implications for geophysical measurements, *Sci. Rep.,* **10,** 1669.

Grissemann, C., 1971. *Untersuchung der Komplexen Leitfähigkeit und der Dielektrizitätskonstanten Erzhaltiger Gesteine an Gesteinsmodellen. PhD thesis*, University of Innsbruck, Austria.

Gurin, G., Tarasov, A., Ilyin, Y. & Titov, K., 2013. Time domain spectral induced polarization of disseminated electronic conductors: laboratory data analysis through the Debye decomposition approach, *J. Appl. Geophys.,* **98,** 44–53.

Gurin, G., Titov, K., Ilyin, Y. & Tarasov, A., 2015. Induced polarization of disseminated electronically conductive minerals: a semi-empirical model, *Geophys. J. Int.,* **200,** 1555–1565

Hupfer, S., Martin, T., Weller, A., Günther, T., Kuhn, K., Ngninjio, V.D.N. & Noell, U., 2016. Polarization effects of unconsolidated sulphide-sand-mixtures, *J. Appl. Geophys.,* **135,** 456–465.

Kreith, D., Zhang, Z., Breede, K., Weller, A. & Bücker, M., 2025. Modelling of spectral induced-polarization measurements on cm-sized metallic spheres in sand-water-mixtures, *Geophys. J. Int.,* **242,** 1–17.

Maineult, A., 2016. Estimation of the electrical potential distribution along metallic casing from surface self-potential profile, *J. Appl. Geophys.,* **129,** 66–78.

Maineult, A., 2018. Corrigendum: 'upscaling of spectral induced polarization response using random tube networks', by Maineult et al. (Geophysical Journal International, 209, pp.948–960), *Geophys. J. Int.,* **213,** 1296–1296.

Maineult, A., Jougnot, D. & Revil, A., 2018. Variations of petrophysical properties and spectral induced polarization in response to drainage and imbibition: a study on a correlated random tube network, *Geophys. J. Int.,* **212,** 1398–1411.

Maineult, A., Revil, A., Camerlynck, C., Florsch, N. & Titov, K., 2017. Upscaling of spectral induced polarization response using random tube networks, *Geophys. J. Int.,* **209,** 948–960.

Martin, T. & Weller, A., 2023. Superposition of induced polarization signals measured on pyrite–sand mixtures, *Geophys. J. Int.,* **234,** 699–711.

Mendieta, A., Maineult, A., Leroy, P. & Jougnot, D., 2023. Spectral induced polarization of heterogeneous non-consolidated clays, *Geophys. J. Int.,* **233,** 436–447.

Nelder, J.A. & Mead, R., 1965. A simplex method for function minimization, *Comput. J.,* **7,** 308–313.

Nordsiek, S. & Weller, A., 2008. A new approach to fitting induced-polarization spectra, *Geophysics,* **73,** F235–F245.

Pelton, W.H., Sill, W.R. & Smith, B.D., 1983. Interpretation of complex resistivity and dielectric data—part 1, *Geophys. Trans.,* **29,** 297–330.

Pelton, W.H., Ward, S.H., Hallof, P.G., Sill, W.R. & Nelson, P.H., 1978. Mineral discrimination and removal of inductive coupling with multifrequency IP, *Geophysics,* **43,** 588–609.

Placencia-Gómez, E., Slater, L., Ntarlagiannis, D. & Binley, A., 2013. Laboratory SIP signatures associated with oxidation of disseminated metal sulphides, *J. Contam. Hydrol.,* **148,** 25–38.

Revil, A., Florsch, N. & Mao, D., 2015. Induced polarization response of porous media with metallic particles—part 1: a theory for disseminated semiconductors, *Geophysics,* **80,** D525–D538.

Seigel, H., Nabighian, M., Parasnis, D.S. & Vozoff, K. 2007. The early history of the induced polarization method, *The Leading Edge,* **26,** 312–321.

Stebner, H., Halisch, M. & Hördt, A., 2017. Simulation of membrane polarization of porous media with impedance networks, *Near Surf. Geophys.,* **15,** 563–578

Weller, A. & Slater, L., 2022. Ambiguity in induced polarization time constants and the advantage of the Pelton model, *Geophysics,* **87,** E393–E399.

Wong, J., 1979. An electrochemical model of the induced-polarization phenomenon in disseminated sulfide 635 ores, *Geophysics,* **44,** 1245–1265.

APPENDIX: REMOVAL OF THE HIGH FREQUENCY TREND

At frequencies larger than about 1 kHz, IP spectra can be subjected to a divergence of their imaginary part, due to the classical dielectric behaviour and/or to experimental electromagnetic noise (for instance due to induction between cables). To remove this trend, we modelled the measured raw data ρ^*_{meas} using:

$$\rho^*_{\text{mod}} = \left\{ \left[\rho_0 \left(1 - \sum_{k=1}^{N} m_k \left(1 - \frac{1}{1 + (i\omega\tau_k)^{c_k}} \right) \right) \right]^{-1} + i\omega K \right\}^{-1}, \tag{A1}$$

K being positive or negative, and $N = 1$ for the monomodal samples, $N = 2$ for the bimodal samples. The parameters ρ_0, m_k, τ_k, c_k and K are obtained by an optimization procedure (simulated annealing followed by simplex method to minimize the difference between ρ^*_{mod} and ρ^*_{meas}). We then simply removed the term $i\omega K$ from the raw data ρ^*_{meas} to obtain the corrected data ρ^*_{corr}, as:

$$\rho^*_{\text{corr}} = \left\{ \frac{1}{\rho^*_{\text{meas}}} - i\omega K \right\}^{-1}. \tag{A2}$$

Fig. A shows an example of application of this procedure.

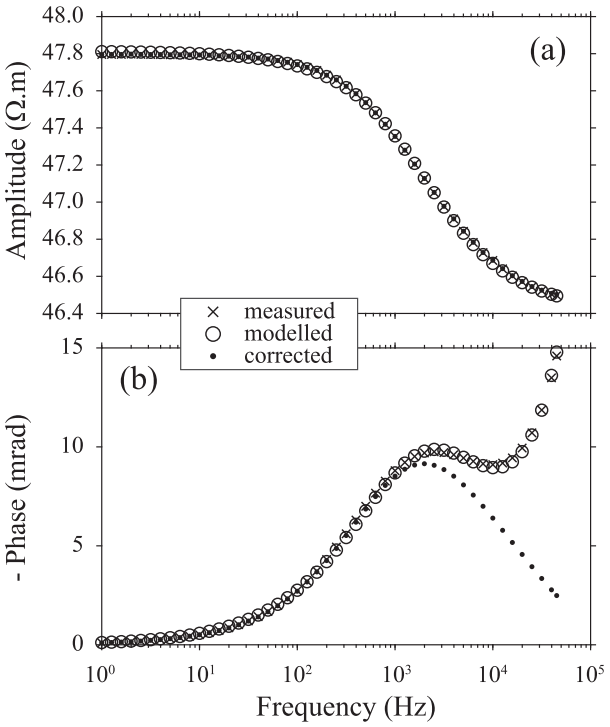

Figure A. Example of SIP spectra correction (sample C02).